ACS APPLIED MATERIALS & INTERFACES

Research Article

www.acsami.org

In Vitro Biocompatibility of Surface-Modified Porous Alumina Particles for HepG2 Tumor Cells: Toward Early Diagnosis and Targeted Treatment

Elisabet Xifre-Perez,[†] Sandra Guaita-Esteruelas,[‡] Malgorzata Baranowska,[†] Josep Pallares,[†] Lluis Masana,[‡] and Lluis F. Marsal*[,†]

[†]Departament d'Enginyeria Electrònica, Elèctrica i Automàtica, Universitat Rovira i Virgili, Avinguda Països Catalans 26, 43007 Tarragona, Spain

[‡]Unitat de Recerca en Lípids i Arteriosclerosi—IISPV, Universitat Rovira i Virgili, C/Sant Llorenç, 21, 43201 Reus, Spain

Supporting Information

ABSTRACT: Porous alumina photoluminescence-inherent particles are produced and proposed for the development of biomarkers detectors and localized treatment of HepG2 cells. Nanoporous alumina particles (NPAPs) are amorphous, consist of hexagonally ordered nanometric pores in an alumina matrix, have high chemical stability in physiological pH, and exhibit a high inherent photoluminescence in the visible spectrum independently of their size, selectable from nanometers to tens of micrometers. The surface of NPAPs is chemically modified using two different functionalization methods, a multistep method with (3-aminopropyl)triethoxysilane (APTES) and glutaraldehyde (GLTA) and a novel simplified-step method with silane-PEG-NHS. Fourier Transform infrared spectroscopy analysis confirmed the proper surface modification of the particles for both functionalization methods. HepG2 cells were cultured during different times with growing concentrations of particles. The analysis of cytotoxicity and cell viability of HepG2 cells confirmed the good biocompatibility of NPAPs in all culture conditions. The results prove the suitability of NPAPs for developing new label-free biomarker detectors and advantageous carriers for localized drug delivery.

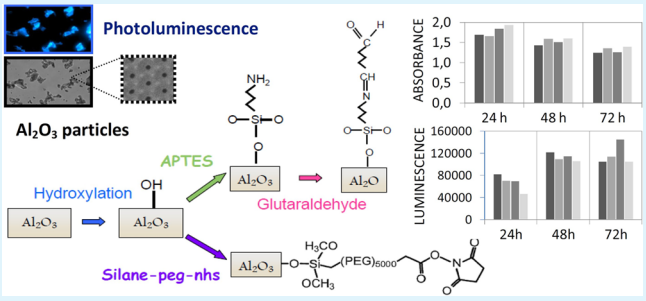

KEYWORDS: *nanoporous alumina particles, liver cancer, biocompatibility, in vitro, photoluminescence, functionalization*

1. INTRODUCTION

Cancer is a leading cause of death worldwide, accounting for 8.2 million deaths in 2012.[1] There are two big problems to address this important pathology; the first one is the early detection of cancer and the second one is the targeted treatment. The early detection of cancer is, in many cases, the key to reducing the mortality.[2]

Conventional cancer treatments such as cisplatin, 5-FU, paclitaxel, vinblastine, and doxorubicin are useful in some types of cancer treatment but they have high side effects and limited accessibility to the tumor tissue.[3−10] Moreover, these current drugs have an unspecific action in healthy cells. For these reasons, there are huge efforts in the development of novel, specific, and targeted therapies for avoiding these adverse effects.[11−13]

Nanoparticles have received considerable interest in recent years, especially with respect to their potential utilization in the field of cancer diagnosis and therapy. The functionalization of the nanoparticles allows their use as agents for theranostics, the perfect combination of therapy and diagnosis.[14] The use of particles for biological applications has been an important breakthrough in recent years.[15−19] Several materials have been used for the formation of particles for biological applications: gold,[20] copper,[21] silver,[22] polymers,[23] silica,[24] titanium oxide,[25] graphite oxide,[26] and porous silicon.[27] The shape of particles made of these materials is diverse, e.g., nanorods, colloids, or irregular structures. However, many of these materials have significant drawbacks for being used in biological applications: they require expensive and complex installations for manufacturing, they are not fully biocompatible or their morphology is altered in physiological pH, they have no intrinsic fluorescence (need to be dyed for their use as biomarker detector), or they are not porous. Porosity gives added value to particles since the larger effective surface area of porous particles endows high capacity for drug storage and drug release at different rates.[28]

Here we propose porous alumina for the production of particles for biological applications. Porous alumina is a material commonly used in nanotechnology for developing optical and electrical devices.[29−31] Due to its chemical, physical, and optical properties, porous alumina can be an excellent material for the fabrication of porous particles for biological applications. Some of these interesting properties are its highly stable morphology at physiological pH, tunable porous structure, cost-effective

Received: June 7, 2015
Accepted: August 4, 2015
Published: August 4, 2015

ACS Publications © 2015 American Chemical Society

DOI: 10.1021/acsami.5b05016
ACS Appl. Mater. Interfaces 2015, 7, 18600−18608

fabrication, and nontoxicity.[32−36] Especially remarkable is its high effective surface area, chemically modifiable with organic compounds,[37] that makes of porous alumina an advantageous carrier for localized drug delivery.[38] Furthermore, another singular characteristic distinguishes porous alumina from most materials: its inherent photoluminescence in the visible spectrum range. This makes of porous alumina an exceptional material for developing new label-free biomarker detectors.[39]

Porous alumina consists of nanometric pores hexagonally arranged in an alumina matrix. Its geometric characteristics, such as pore size, interpore distance, porosity, and thickness, can be controlled by the anodization conditions (voltage and time of anodization, temperature, and acid used as electrolyte, and so on).[40] We precisely control porous alumina manufacturing methods.[41−43] Thereby we obtain porous structures with the appropriate morphology to meet any application needs.

The work that we present here is part of our long-term research goal: the technological development of nanoporous alumina particles (NPAPs) as selective label-free biomarker detector and drug carriers for the detection and treatment of cancer cells. In order to successfully achieve this final objective, several circumstances and steps must be overcome: NPAPs must be biocompatible, their intrinsic photoluminescence must be easily observed by commonly used microscopic equipment, and NPAPs must be successfully functionalized for increasing their selectivity to biomarkers and localized drug delivery.

In this work, we show the successfully completed phases of fabrication, characterization, and functionalization of NPAPs. Two different methods of functionalization are presented and verified by spectroscopic methods. We also evaluate the simplified process for linking a protein/antibody to NPAPs by electrostatic attraction. Finally, we demonstrate the biocompatibility of NPAPs by incubating HepG2 cells with several particle concentrations and analyzing cell viability and cytotoxicity.

2. EXPERIMENTAL SECTION

Materials. High-purity aluminum foils (99,999%) were purchased from Goodfellow Cambridge Ltd. (UK). Glutaraldehyde (anhydrous 10% in EtOH) was purchased from Electron Microscopy Science (U.S.). Silane-PEG-NHS was obtained from Nanocs (U.S.). Oxalic acid, perchloric acid, chromic acid, hydroxyperoxide, 3-aminopropylotrimethoxysilane, bovine serum albumin (BSA), phosphate buffer saline (PBS), toluene, dimethyl sulfoxide, and ethanol were purchased from Sigma-Aldrich. Milli-Q water with resistivity higher than 18 MΩ·cm was used for rinsing and preparation of solutions. HepG2 cells were purchased from ATCC (LGC Standards S.L.U., Spain) and were growth in MEM plus 10% fetal media from Biowest (LabClinics, Spain). The CellTiter-Glo Luminescent Cell Viability Assay was obtained from Promega and Cytotoxicity Detection Kit (LDH) from Roche Diagnostics.

Fabrication of NPAPs. Highly ordered and large-area nanoporous anodic alumina membranes were prepared by electrochemical anodization of aluminum substrates (99.999% purity) in a two-step anodization process.[43,44] Briefly, the aluminum sheets were first electropolished in a mixture of ethanol (EtOH) and perchloric acid ($HClO_4$; 4:1 (v:v)) at 20 V for 4 min. Then the first anodization step was performed in an aqueous solution of oxalic acid ($H_2C_2O_4$) 0.3 M at 40 V and 6 °C for 15 h. The obtained porous alumina layer with disordered pores was dissolved by wet chemical etching in a mixture of 0.4 M phosphoric acid (H_3PO_4) and 0.2 M chromic acid (H_2CrO_7) at 70 °C for 3 h.[45] The second anodization step was performed under the same anodization conditions as those of the first step until a thick porous alumina layer was obtained. It was detached from the aluminum substrate following the procedure reported elsewhere.[46] The highly ordered porous alumina membrane was ground with a mortar and pestle and ultrasonically treated for obtaining nanometric and micrometric particles. Finally, the size of the particles is selected using standard filtration methods.[38,47,48] The X-ray diffraction of the obtained porous alumina particles shows an amorphous structure (Supporting Information Figure S1).

Functionalization with APTES and GLTA. First, NPAPs were boiled in hydroxyperoxide (H_2O_2) to obtain hydroxyl (-OH) groups on the surface. After 1 h, NPAPs were washed. The washing process of NPAPs at any functionalization step involves the dispersion of the particles in a cleaning agent (water, ethanol, or toluene, etc.), stirring, and shaking to prevent aggregation and the separation from the cleaning agent by centrifugation at 6000 rpm for 15−20 min. After the hydroxylation step, NPAPs were washed twice with Milli-Q water and ethanol and dried in the oven at 100 °C for 2 h to ensure complete drying. The surface of NPAPs must be completely dry as any trace of water may result in silane aggregation, avoiding its attachment to the surface.

NPAPs were then dispersed in a solution with 50 μL of APTES in 5 mL of toluene (1% (v:v) of silane). The solution was vigorously stirred to eliminate aggregates for 1 h followed by 1 h of sonication to remove any polymerized APTES. After this process, the particles were washed with toluene, ethanol (twice) , and Milli-Q water, then dried with nitrogen, and incubated overnight in the oven at 110 °C to cross-link the silane.

APTES-modified NPAPs were then suspended in 10% (v:v) GLTA for 1 h at room temperature, washed with ethanol and Milli-Q water, and dried. At this point, NPAPs have an aldehyde ending (-CHO) surface that can be covalently attached to biomolecules.

Functionalization with Silane-PEG-NHS. NPAPs were boiled in hydroxyperoxide (H_2O_2) to obtain hydroxyl (-OH) groups on the surface in the same conditions as for the APTES-GLTA functionalization. Then the particles were washed with Milli-Q water and ethanol and were dried in the oven at 100 °C for 2 h to ensure their complete drying. After hydroxylation, NPAPs were suspended in freshly prepared 1% (v:v) of silane-PEG-NHS in dimethyl sulfoxide (DMSO) solution. Silane-PEG-NHS left for a long time polymerizes and loses activity. NPAPs were stirred in this solution for 1 h at room temperature, washed with DMSO and Milli-Q water, and dried with nitrogen.

Cell Culture. HepG2 cells were obtained from ATCC. After thawing, the cells were seeded into 75 cm^2 flasks and cultured according to the supplier's recommendations in MEM medium with 1 mM L-glutamine, 1 mM penecillin-streptomicin, and 1 mM NEAA and supplemented with fetal bovine serum (10% (v:v) final concentration). The cells were placed in a humidified incubator at 37 °C and 5% CO_2 until enough cells were available for the experiments.

Viability Analysis. The day before the experiment, HepG2 cells were seeded at 7500 cells/cm^2 in p96 plates. The CellTiter-Glo Luminescent Cell Viability Assay was performed according the manufacturer's protocol. To determine the number of viable cells in culture, the quantitation of the ATP present was detected (Promega).

Cytotoxicity Analysis. The day before the experiment, HepG2 cells were seeded at 10.000 cells/cm^2 in p12 plates. The cytotoxicity assay was performed by analyzing LDH release into the medium using the Cytotoxicity Detection Kit (Roche Diagnostics, Basel, Switzerland).

Environmental Scanning Electron Microscopy. The size, shape, and surface morphology of NPAPs were observed with an environmental scanning electron microscopy (ESEM) FEI Quanta 600 (Hillsboro, OR, USA) under high vacuum with a filament current of 20 eV. Before observation, NPAPs were sputter coated with a 30 nm layer of gold to increase the image quality.

Optical Microscope Images. Cell incubation with NPAPs was observed with an optical inverted microscope Olympus IX71. Phase contrast images were obtained with a halogen lamp whereas for DAPI, fluorescence filters were used. The images were processed with CellF program.

X-ray Diffraction (XRD). XRD measurements were made using a Bruker-AXS D8-Discover diffractometer with parallel incident beam (Göbel mirror) and vertical $\theta-\theta$ goniometer, XYZ motorized stage mounted on an Eulerian cradle, diffracted-beam Soller slits, a 0.2° receiving slit, and a scintillation counter as a detector. The angular 2θ diffraction range was between 5 and 70°. The data were collected with an

DOI: 10.1021/acsami.5b05016
ACS Appl. Mater. Interfaces 2015, 7, 18600−18608

angular step of 0.05° at 3 s/step. Cu K radiation was obtained from a copper X-ray tube operated at 40 kV and 40 mA.

Photoluminescence Spectrum. Photoluminescence spectra were performed using a fluorescence spectrophotometer from Photon Technology International Inc. (Birmingham, NJ, USA) with a Xe lamp used as the excitation light source.

Fourier Transform Infrared Spectrometry. Covalent bounds of functionalized NPAPs were investigated using a Fourier-transform infrared (FTIR) spectrometer Bruker Vertex 70 (Bruker Optics). The transmission spectrum of NPAPs after each functionalization step was measured over the range of 400−4000 cm^{-1} with a resolution of 4 cm^{-1}. Each spectrum is the average of 256 scans. A quartz glass kept dry in a desiccant box was the holder for NPAPs. The transmission spectrum of the glass was measured to obtain the reference spectrum. Then a highly concentrated drop of NPAPs was placed on the glass, and its transmission spectrum was measured when the sample was completely dry.

3. RESULTS AND DISCUSION

Characterization of NPAPs. The surface morphology and shape of NPAPs are presented in Figure 1. Porous alumina

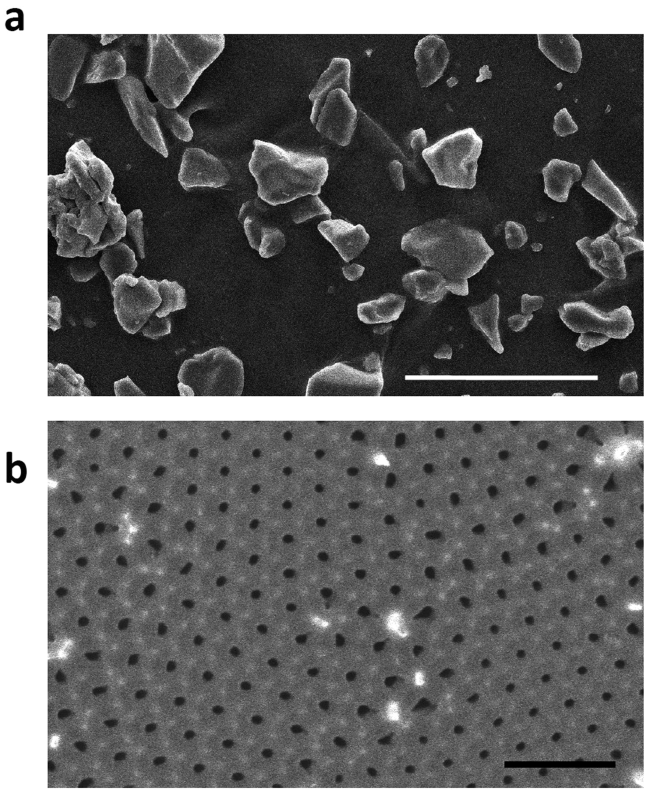

Figure 1. (a) SEM image of NPAPs. Scale bar: 100 μm. (b) Magnification of NPAPs surface. Scale bar: 300 nm.

consists of an alumina matrix with a hexagonally ordered distribution of pores with a very high degree of ordering. The diameter of the pores is approximately 20 nm, and the interpore distance is 100 nm. The shape of NPAPs is irregular, and their size ranges from the nanometric scale (a few nanometers) up to approximately 25 μm. This wide range of sizes allows the easy selection (by filtering) of a reduced size range to meet any application requirements.

NPAPs present an inherent photoluminescence independently of their size that can be easily observed with conventional optical equipment such as an optical microscope equipped with fluorescence filters in the DAPI range (Figure 2a). The photoluminescence spectrum of NPAPs is observed in Figure 2b for

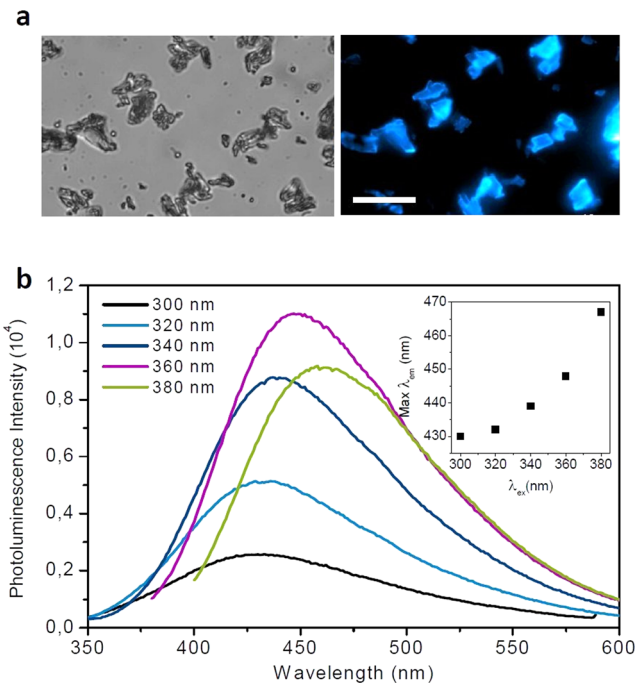

Figure 2. (a) Bright-field and blue fluorescence field image (DAPI filters) of a representative sample of NPAPs. Scale bar: 3 μm. (b) Photoluminescence spectrum of NPAPs for different excitation wavelengths between 300 and 380 nm. Inset: maximum emission wavelength (λ_{em}) of NPAPs for the different excitation wavelengths (λ_{ex}).

different excitation wavelengths. When NPAPs are excited in the UVA range, a broad photoluminescence peak is observed in the visible range. This inherent photoluminescence of the material is very stable and is not significantly affected by the subsequent functionalization steps (Supporting Information Figure S3).[49] The wavelength at which photoluminescence emission is maximum slightly shifts to the red with the excitation wavelength although it remains within the blue range. The maximum photoluminescence emission of NPAPs is obtained at λ = 448 nm for the excitation wavelength 360 nm. This inherent photoluminescence in the visible range makes of NPAPs very appropriate candidates for developing label-free biomarker detectors.

Functionalization of NPAPs. Functionalization increases the affinity of a surface to specific proteins.[50,51] Common functionalization procedures use silane compounds with terminal functional groups that interact electrostatically or covalently with protein surface groups, increasing protein binding. Functionalization of the NPAPs will increase their selectively and linking to specific biological agents.

The NPAPs surface was modified using two different functionalization processes, illustrated in Scheme 1. One process is based on (3-aminopropyl)triethoxysilane (APTES) and glutaraldehyde (GLTA), involving several functionalization steps. In order to simplify the functionalization process of NPAPs, another process that uses silane-PEG-NHS as linker is also presented. FTIR spectroscopy was used to efficiently verify the modification of the NPAPs surface after the different functionalization processes.

a. Functionalization with APTES + GLTA. The surface of NPAPs was modified with the two-step method consisting of APTES and GLTA.[52−54] The silane end of the APTES molecule binds covalently to hydroxyl groups generated on the NPAPs

DOI: 10.1021/acsami.5b05016
ACS Appl. Mater. Interfaces 2015, 7, 18600−18608

Scheme 1. Chemical Structures at the Different Steps of the Functionalization Processes: APTES + GLTA and silane-PEG-NHS

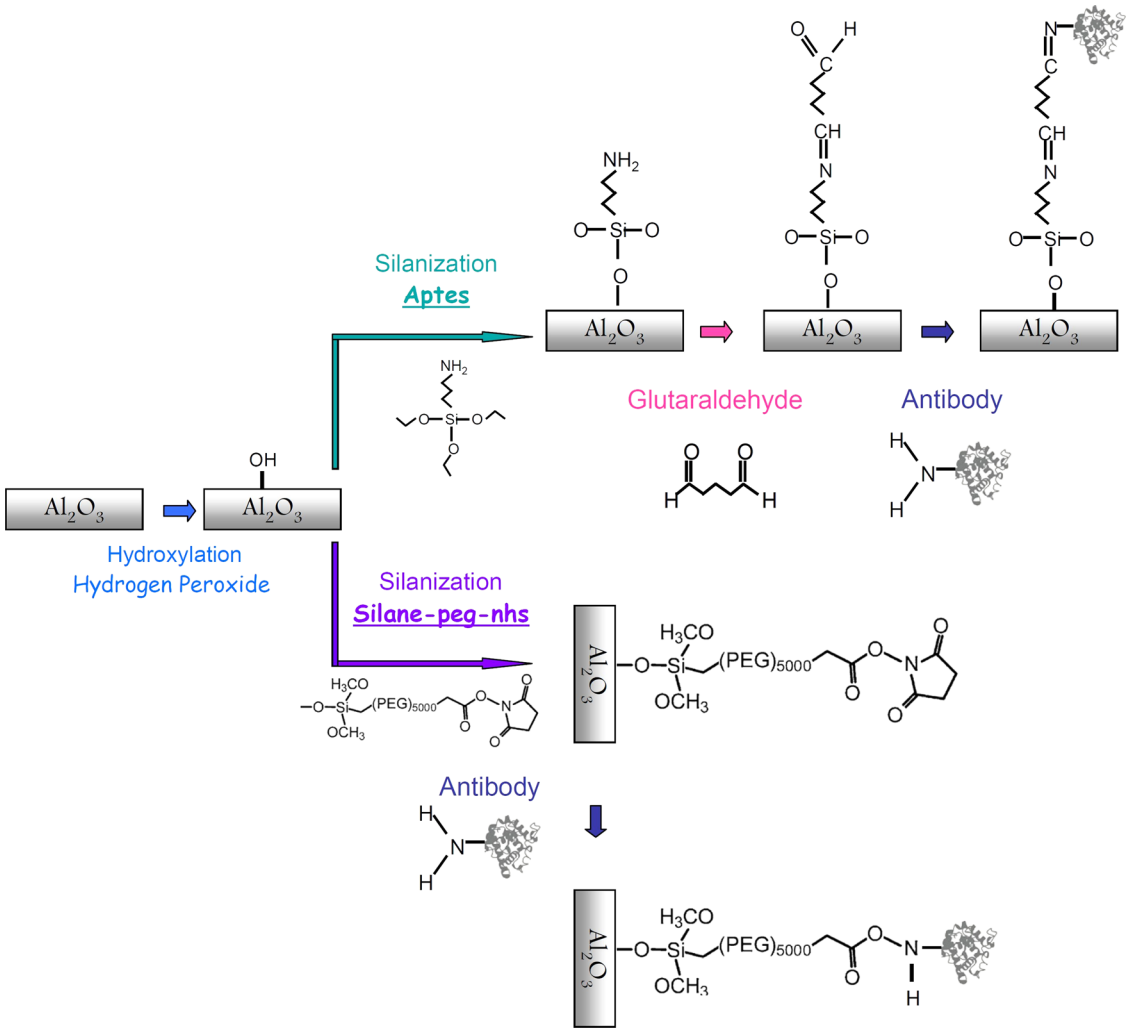

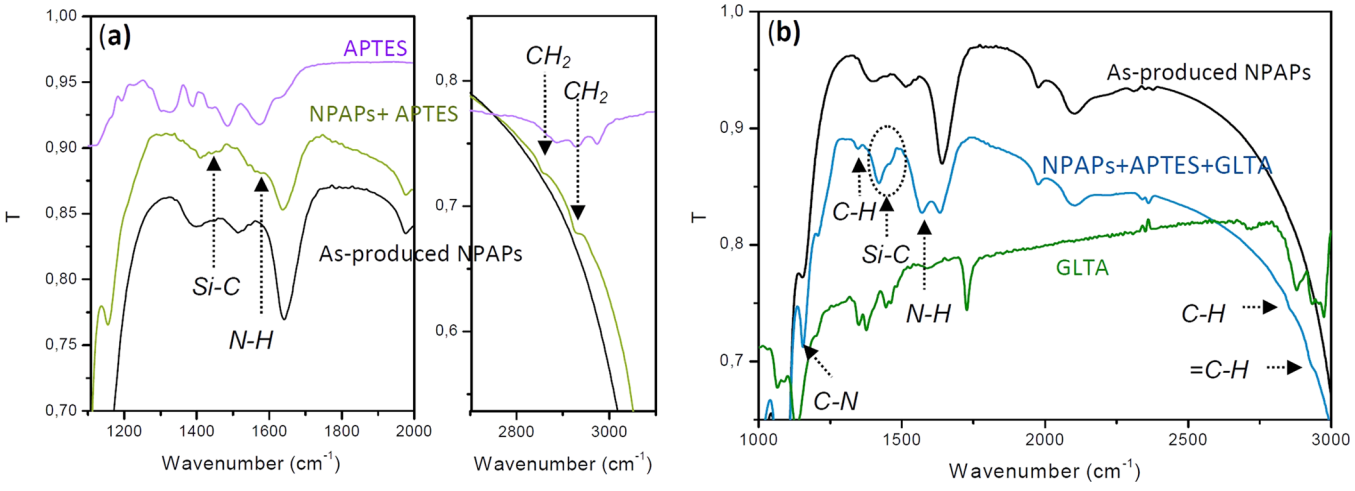

Figure 3. FTIR transmission spectrum of as-produced NPAPs and NPAPs functionalized with APTES (a) and GLTA (b). Transmission spectra of pure APTES and pure GLTA are also presented for comparison.

surface with the hydroxylation step, and the amino end of the molecule increases protein adsorption to the surface through electrostatic interactions. The linear GLTA molecule is terminated at both ends by aldehyde groups and thus may be used to transform surface amino groups to surface aldehyde groups. These aldehyde groups covalently bind proteins through the Schiff base reaction.[55]

First of all, the FTIR transmittance spectrum of NPAPs with no treatment or modification (as-produced) was measured for reference (Figure 3a). Three peaks are identified at this

DOI: 10.1021/acsami.5b05016
ACS Appl. Mater. Interfaces 2015, 7, 18600−18608

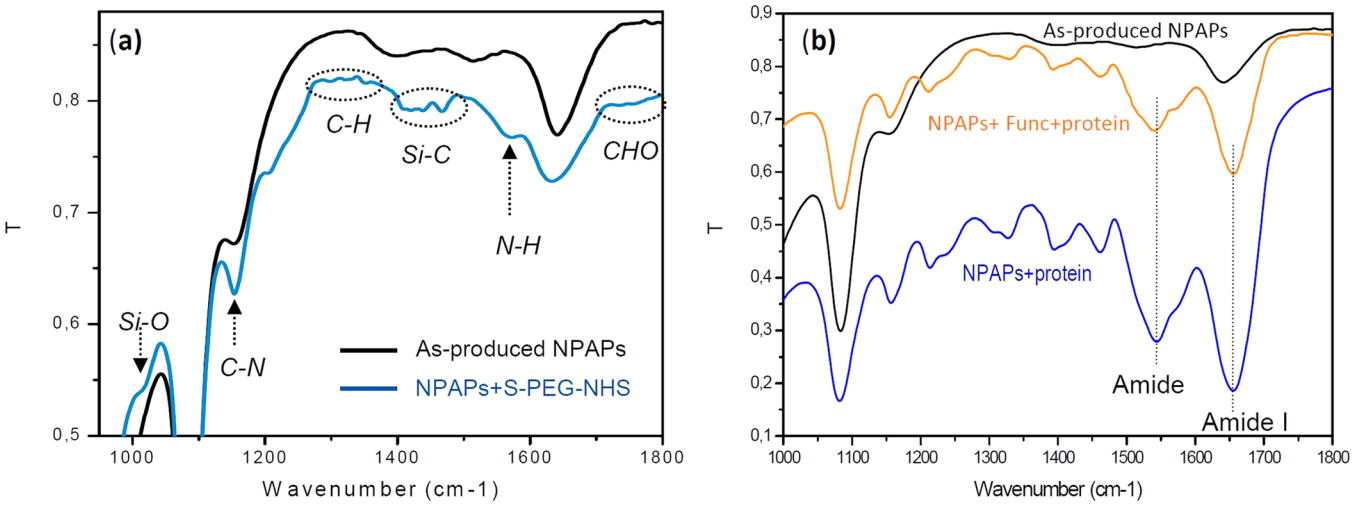

Figure 4. (a) FTIR transmission spectrum of as-produced NPAPs and NPAPs functionalized with silane-PEG-NHS. (b) FTIR transmission spectrum of as-produced NPAPs, NPAPs with BSA immobilized on their surface by adsorption (protein), and NPAPs with BSA covalently attached due to the previous functionalization of the surface (func + protein). The spectra are shifted on the *y*-axis for clarity.

transmittance spectrum (1082, 1400, and 1641 cm^{-1}), which are assigned to the alumina longitudinal phonon adsorption band.[56] The broad bands that appear in the range from 800 to 1000 cm^{-1} are characteristic of aluminum oxide.[56,57]

The surface modification of NPAPs with APTES is confirmed with the analysis of the FTIR transmission spectrum in Figure 3a. The spectrum of pure APTES is also shown for comparison. According to literature,[58] vibrational peaks belonging to particular molecular groups can be identified. A characteristic band of amine−NH_2 terminal groups occurring at 1578 cm^{-1} in APTES is present in the functionalized NPAPs spectrum at the same wavenumber, assigned to (-N−H) bending vibration.[59] The bending vibration of -C−Si- is observable at 1440 cm^{-1}. Analyzing the spectra for higher wavenumber values, two methylene vibrational peaks are observed at 2928 and 2860 cm^{-1} in the functionalized NPAPs spectrum. They are ascribable to asymmetric and symmetric CH_2 stretching, respectively.[58]

The next functionalization step with GLTA was also analyzed with FTIR spectroscopy (Figure 3b). The most important structural information in terms of the APTES + GLTA adsorption is observed mainly in the range from 1100 to 1600 cm^{-1}. The bending vibrations from -C−N are identified at 1155 cm^{-1}. The transmittance minimum at 1350 cm^{-1} corresponds to the alkane bond C−H, and the other two minimums at 1422 and 1459 cm^{-1} represent Si−C bonds.[60] The presence of the amide bond (N−H) is confirmed at 1570 cm^{-1}. For higher wavenumbers, we can observe the presence of stretching vibrations from (=C−H-) at 2805 cm^{-1} and from (-C−H-) at 2940 cm^{-1}.

b. Functionalization with Silane-PEG-NHS. Silane-PEG-NHS has been reported recently as a successful linker for porous alumina surface functionalization[60] and simplifies the process by reducing the number of functionalization steps. The functionalization with silane-PEG-NHS has the ability to attach only one molecule of protein forming a thin single-molecule layer on the NPAPs surface. This is important in single-molecule studies as well as for obtaining homogeneous layers of proteins.

The functionalization of the NPAPs surface with silane-PEG-NHS is confirmed with the analysis of the FTIR transmission spectrum (Figure 4a). This figure also shows the transmission spectrum of as-produced NPAPs for comparison. At 1013 cm^{-1}, it is possible to notice bending vibrations from -Si−O-. A wide peak with minimum at 1153 cm^{-1} corresponding to bending vibrations from -C−N- is also observed. Peaks for the -C−H- group at 1286−1355 cm^{-1} are visible as well as bending vibrations of -Si−C- can be identified at 1407−1440 cm^{-1}. Additional vibrations from -N−H- amide are observed at 1574 cm^{-1}. Finally, the presence of the aldehyde group (-CHO) is confirmed at 1722−1799 cm^{-1}.[56]

Immobilization of BSA on the Surface of As-Produced and Functionalized NPAPs. The immobilization of proteins or antibodies on the NPAPs surface is important for their application in biological processes. In previous sections, two different functionalization processes for covalently linking NPAPs and protein have been presented and confirmed with spectroscopic methods. However, the functionalization process requires several steps for being completed, three in the case of APTES and GLTA or two for the case of silane-PEG-NHS.

Strong NPAPs−protein bonding can also be obtained by adsorption. Adsorption of the protein/antibody to the surface of NPAPs is especially stable due to the attracting electrostatic interaction between NPAPs and protein. For studying the direct NPAPs−protein linking, bovine serum albumin (BSA) protein was linked to NPAPs by adsorption. The transmission spectrum of these NPAPs is compared to that of NPAPs covalently linked to BSA using the APTES and GLTA functionalization process (Figure 4b). At first glance we can observe that the transmission spectrum of the tandem BSA-NPAPs obtained both by adsorption and by functionalization presents the same shape. This means that the vibrational peaks belonging to particular molecular groups are closely similar for both linking processes. Besides, the bonding of the protein to the NPAPs is also demonstrated by the identification of the amide I and II bands of the protein at the transmission spectrum of NPAPs. The minimum of transmission at 1652 cm^{-1} is assigned to the amide I band.[61,62] Amide I absorption originates from the C=O stretching vibration of the amide group (coupled to in-phase bending of the N−H bond and stretching of the C−N bond). Around 1540 cm^{-1} we identify the amide II band.[63,64] Amide II comes from the N−H bending and C−N stretching vibrations.

The strong adsorbance of the protein to the NPAPs surface is explained as a consequence of several processes, prevailing the electrostatic attraction between protein and particle.

DOI: 10.1021/acsami.5b05016
ACS Appl. Mater. Interfaces 2015, 7, 18600−18608

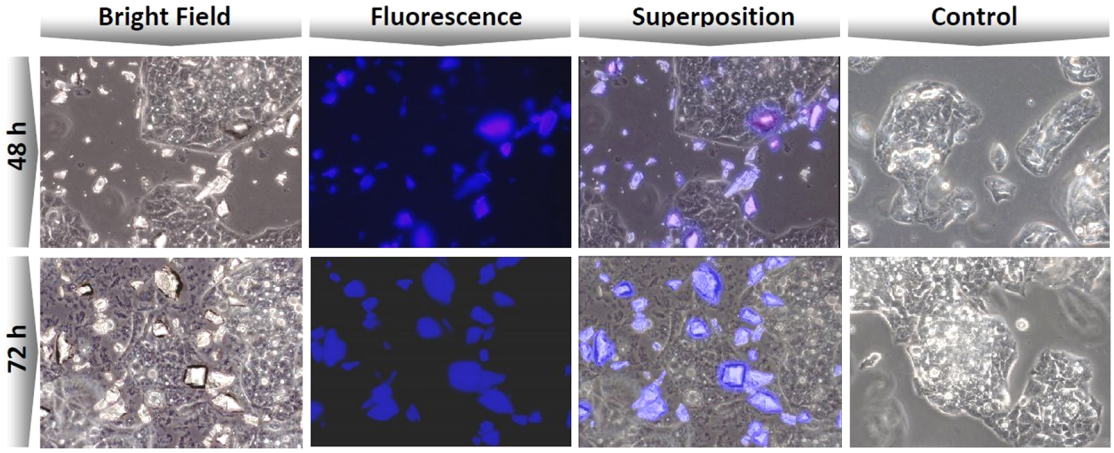

Figure 5. Microscope images of HepG2 cells incubated 48 and 72 h with NPAPs: bright field, blue fluorescence field and superposition of both fields. Control (cells incubated with no NPAPs) is also presented for comparison (bright field).

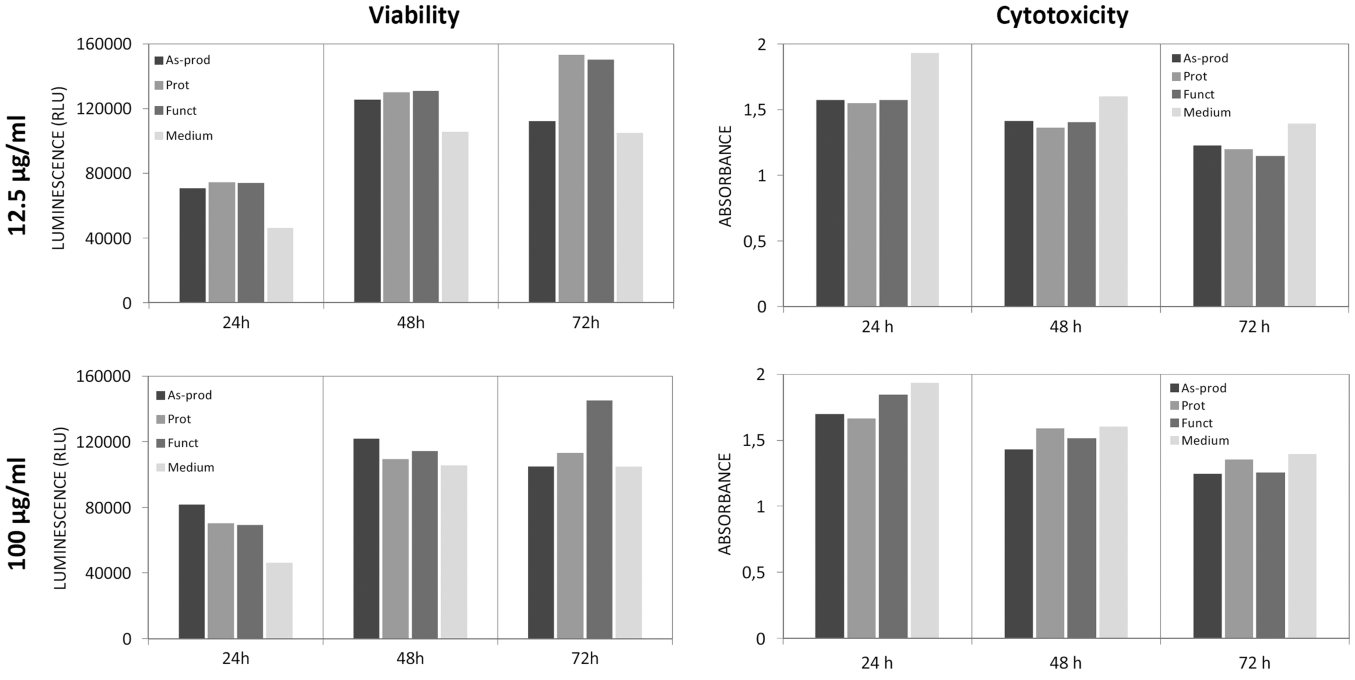

Figure 6. Cytotoxicity and viability of HepG2 cells incubated with as-produced, functionalized, and direct protein linked NPAPs for concentrations of 12.5 and 100 μg/mL within 24, 48, and 72 h. Cytotoxicity and viability of cells incubated with no NPAPs (medium) are also presented for comparison.

The isoelectric point (IEP) of BSA is 4.7,[65] and its ζ potential at physiological pH is highly negative.[66] On the contrary, the measured ζ potential of NPAPs at the same pH is highly positive (Supporting Information Figure S2), promoting its strong electrostatic attraction to the protein. The ζ potential magnitude of NPAPs also indicates that they are electrically stable and resist aggregation. Besides, the van der Waals interaction between protein and particle together with hydrogen bond effects participate for the strong adsorption of the protein to NPAPs.

Cytotoxicity and Cell Viability of HepG2 Cells. An ideal particle for cancer detection and treatment should have good biocompatibility or low cytotoxicity. In order to check the biocompatibility of NPAPs, cell viability and cytotoxicity assays have been performed.

To determine the number of viable cells in culture, ATP quantification assay in HepG2 cell was made. The levels of ATP signal the presence of metabolically active cells. Moreover, to analyze cytotoxicity, LDH release was quantified.

HepG2 cells were incubated with 100 and 12.5 μg/mL of NPAPs, and the cell viability and cytotoxicity at 24, 48, and 72 h were analyzed.

Figure 5 shows the fluorescence images of the HepG2 cells cultured with NPAPs for 48 and 72 h. The NPAPs can be clearly identified due to its photoluminescence. Their presence in the culture medium does not affect the HepG2 normal growth.

As-produced NPAPs were incubated with HepG2 cells, and cell viability and cytotoxicity were analyzed. Vehicle was used as a control (Figure 6). We did not observe any significant difference between our as-produced NPAPs compared to functionalized NPAPs in the cytotoxicity assays or control. Furthermore, we did not find differences between all incubation times.

In the viability assay of HepG2 cells, we did not show any significant difference between as-produced NPAPs, functionalized

DOI: 10.1021/acsami.5b05016
ACS Appl. Mater. Interfaces 2015, 7, 18600−18608

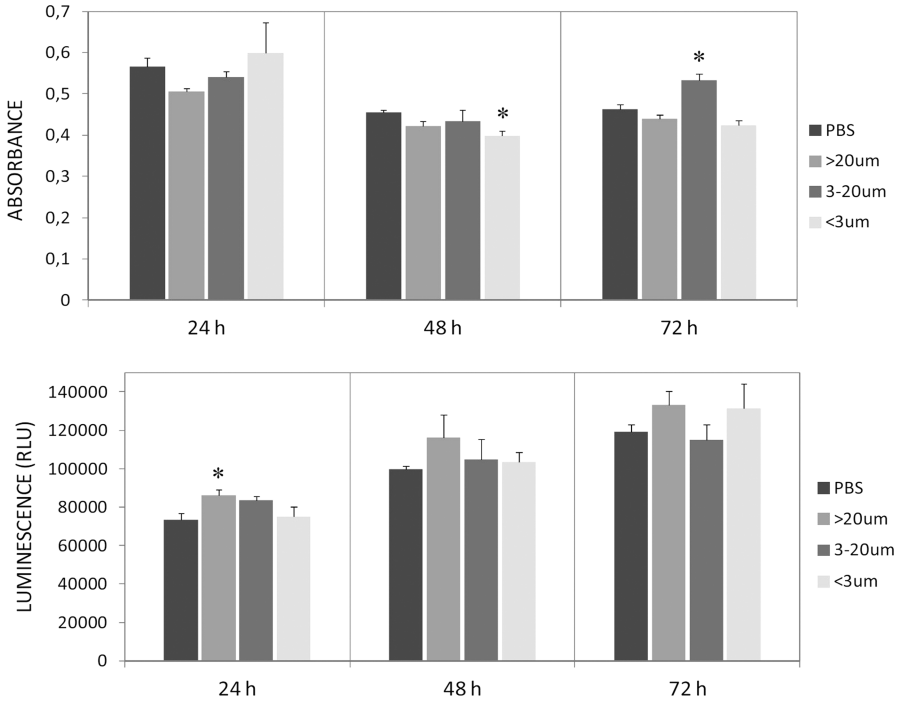

Figure 7. LDH analysis (top) and viability analysis (bottom) at 24, 48, and 72 h for HepG2 cells incubated with several sizes of NPAPs. The LDH and viability analyses for cells incubated with no NPAPs (PBS) are also presented for comparison.

NPAPs, or control conditions. Once again, we did not observed distinctiveness between all incubation times.

The analysis of the cell viability indicates that our as-produced NPAPs do not negatively affect the HepG2 cells. In the same direction, the cytotoxicity assay does not show any change between all growing conditions (Figure 6).

The influence of the NPAPs size on the biocompatibility of HepG2 cells has also been analyzed. By filtration three different size ranges have been selected for the analysis: <3, 3−20, and >20 μm. HepG2 cell were cultured with all NPAPs sizes at 100 μg/mL, and the cytotoxicity and cell viability were analyzed at different times (Figure 7).

In cytotoxicity experiments, we could observe significant differences in NPAPs of <3 μm at 48 h of treatment and 3−20 μm at 72 h versus control conditions.

By the other hand, analyzing the cell viability we could find a significant difference in the NPAPs of >20 μm at 24 h versus control conditions. In the other growing conditions we could not observe any change.

The results demonstrate that the cytotoxicity and viability presented by the cells are very similar to the results obtained in control conditions regardless of the size of NPAPs.

4. CONCLUSIONS

The application of NPAPs for the identification and treatment of HepG2 cells has been assessed. The surface of NPAPs was successfully modified with a commonly used functionalization method consisting of APTES and GLTA. Besides this method, a very recently used functionalization consisting of silane-PEG-NHS was successfully carried out. The surface modification with silane-PEG-NHS simplifies the process and reduces the number of functionalization steps. Besides, the immobilization of BSA on NPAPs by adsorption was assessed. The strong electrostatic attraction between BSA-NPAPs was successfully exploited, and a strong link between them was obtained.

HepG2 cells were cultured with different NPAPs concentrations for 24, 48, and 72 h. The viability and cytotoxicity analysis carried out for all of these culture conditions demonstrates the biocompatibility of NPAPs and their suitability for biological applications.

■ ASSOCIATED CONTENT

Supporting Information

The Supporting Information is available free of charge on the ACS Publications website at DOI: 10.1021/acsami.5b05016.

X-ray diffraction, ζ potential, and photoluminescence of porous anodic alumina before and after the functionalization steps (PDF)

■ AUTHOR INFORMATION

Corresponding Author

*E-mail: lluis.marsal@urv.cat.

Notes

The authors declare no competing financial interest.

■ ACKNOWLEDGMENTS

This work was supported by the Spanish Ministry of Economy and Competitiveness (MINECO) under Grant No. TEC2012-34397, by the Catalan Government under Project 2014 SGR 1344, by the ICREA under the ICREA Academia Award, and by University Rovira i Virgili, Banco Santander and the Catalan Government under Project 2013URV-LINE05.

■ REFERENCES

(1) *Globocan 2012: Estimated Cancer Incidence, Mortality and Prevalence Worldwide in 2012*; International Agency for Research on Cancer, World Health Organization: Lyon, France, 2012.

(2) Hussain, T.; Nguyen, Q. T. Molecular Imaging for Cancer Diagnosis and Surgery. *Adv. Drug Delivery Rev.* **2014**, *66*, 90−100.

DOI: 10.1021/acsami.5b05016
ACS Appl. Mater. Interfaces 2015, 7, 18600−18608

(3) Chabner, B. A.; Roberts, T. G. Chemotherapy and the War on Cancer. *Nat. Rev. Cancer* **2005**, *5*, 65−72.
(4) Sio, T. T.; Ko, J.; Gudena, V. K.; Verma, N.; Chaudhary, U. B. Chemotherapeutic and Targeted Biological Agents for Metastatic Bladder Cancer: A Comprehensive Review. *Int. J. Urol.* **2014**, *21*, 630−637.
(5) Zheng, Y.; Dou, Y.; Duan, L.; Cong, C.; Gao, A.; Lai, Q.; Sun, Y. Using Chemo-Drugs or Irradiation to Break Immune Tolerance and Facilitate Immunotherapy in Solid Cancer. *Cell. Immunol.* **2015**, *294*, 54−59.
(6) Li, E.; Subramanian, J.; Anderson, S.; Thomas, D.; Mckinley, J.; Jacobs, I. A. Development of Biosimilars in an Era of Oncologic Drug Shortages. *Drug Des., Dev. Ther.* **2015**, *9*, 3247−3255.
(7) Mehmood, R. K. Review of Cisplatin and Oxaliplatin in Current Immunogenic and Monoclonal Antibody Treatments. *Oncol. Rev.* **2014**, *8*, 256.
(8) Khaderi, S.; Guiteau, J.; Cotton, R. T.; O'Mahony, C.; Rana, A.; Goss, J. A.; Saira. Role of Liver Transplantation in the Management of Hepatoblastoma in the Pediatric Population. *World J. Transplant.* **2014**, *4*, 294−298.
(9) Fernandes, E.; Ferreira, J. A.; Andreia, P.; Luis, L.; Barroso, S.; Sarmento, B.; Santos, L. L. New Trends in Guided Nanotherapies for Digestive Cancers: A Systematic Review. *J. Controlled Release* **2015**, *209*, 288−307.
(10) Pérez-Herrero, E.; Fernández-Medarde, A. Advanced Targeted Therapies in Cancer: Drug Nanocarriers, the Future of Chemotherapy. *Eur. J. Pharm. Biopharm.* **2015**, *93*, 52−79.
(11) Parveen, S.; Sahoo, S. K. Polymeric Nanoparticles for Cancer Therapy. *J. Drug Target* **2008**, *16*, 108−123.
(12) Grinberg, S.; Linder, C.; Heldman, E. Progress in Lipid-Based Nanoparticles for Cancer Therapy. *Crit. Rev. Oncog.* **2014**, *19*, 247−260.
(13) Prabhu, R. H.; Patravale, V.; Joshi, M. D. Polymeric Nanoparticles for Targeted Treatment in Oncology: Current Insights. *Int. J. Nanomed.* **2015**, *10*, 1001−1018.
(14) Key, J.; Kim, Y.-S.; Tatulli, F.; Palange, A. L.; O'Neill, B.; Aryal, S.; Ramirez, M.; Liu, X.; Ferrari, M.; Munden, R.; Decuzzi, P. Opportunities for Nanotheranosis in Lung Cancer and Pulmonary Metastasis. *Clin. Transl. Imaging* **2014**, *2*, 427−437.
(15) Van Lehn, R. C.; Atukorale, P. U.; Carney, R. P.; Yang, Y. S.; Stellacci, F.; Irvine, D. J.; Alexander-Katz, A. Effect of Particle Diameter and Surface Composition on the Spontaneous Fusion of Monolayer-Protected Gold Nanoparticles with Lipid Bilayers. *Nano Lett.* **2013**, *13*, 4060−4067.
(16) Sun, J.; Bi, C.; Chan, H. M.; Sun, S.; Zhang, Q.; Zheng, Y. Curcumin-Loaded Solid Lipid Nanoparticles Have Prolonged in Vitro Antitumour Activity, Cellular Uptake and Improved in Vivo Bioavailability. *Colloids Surf., B* **2013**, *111*, 367−375.
(17) Pratsinis, A.; Hervella, P.; Leroux, J. C.; Pratsinis, S. E.; Sotiriou, G. A. Toxicity of Silver Nanoparticles in Macrophages. *Small* **2013**, *9*, 2576−2584.
(18) Lee, J. S.; Murphy, W. L. Functionalizing Calcium Phosphate Biomaterials with Antibacterial Silver Particles. *Adv. Mater.* **2013**, *25*, 1173−1179.
(19) El-Dakdouki, M. H.; Xia, J.; Zhu, D. C.; Kavunja, H.; Grieshaber, J.; O'Reilly, S.; McCormick, J. J.; Huang, X. Assessing the in Vivo Efficacy of Doxorubicin Loaded Hyaluronan Nanoparticles. *ACS Appl. Mater. Interfaces* **2014**, *6*, 697−705.
(20) Fazal, S.; Jayasree, A.; Sasidharan, S.; Koyakutty, M.; Nair, S. V.; Menon, D. Green Synthesis of Anisotropic Gold Nanoparticles for Photothermal Therapy of Cancer. *ACS Appl. Mater. Interfaces* **2014**, *6*, 8080−8089.
(21) Song, L.; Connolly, M.; Fernández-Cruz, M. L.; Vijver, M. G.; Fernández, M.; Conde, E.; de Snoo, G. R.; Peijnenburg, W. J. G. M.; Navas, J. M. Species-Specific Toxicity of Copper Nanoparticles among Mammalian and Piscine Cell Lines. *Nanotoxicology* **2014**, *8*, 383−393.
(22) Hoppens, M. A.; Sylvester, C. B.; Qureshi, A. T.; Scherr, T.; Czapski, D. R.; Duran, R. S.; Savage, P. B.; Hayes, D. Ceragenin Mediated Selectivity of Antimicrobial Silver Nanoparticles. *ACS Appl. Mater. Interfaces* **2014**, *6*, 13900−13908.
(23) Feng, G.; Li, K.; Liu, J.; Ding, D.; Liu, B. Bright Single-Chain Conjugated Polymer Dots Embedded Nanoparticles for Long-Term Cell Tracing and Imaging. *Small* **2014**, *10*, 1212−1219.
(24) Cheng, Y.-J.; Luo, G.-F.; Zhu, J.-Y.; Xu, X.-D.; Zeng, X.; Cheng, D.-B.; Li, Y.-M.; Wu, Y.; Zhang, X.-Z.; Zhuo, R.-X.; He, F. Enzyme-Induced and Tumor-Targeted Drug Delivery System Based on Multifunctional Mesoporous Silica Nanoparticles. *ACS Appl. Mater. Interfaces* **2015**, *7*, 9078−9087.
(25) Newman, M. D.; Stotland, M.; Ellis, J. I. The Safety of Nanosized Particles in Titanium Dioxide- and Zinc Oxide-Based Sunscreens. *J. Am. Acad. Dermatol.* **2009**, *61*, 685−692.
(26) Wang, I. N. E.; Robinson, J. T.; Do, G.; Hong, G.; Gould, D. R.; Dai, H.; Yang, P. C. Graphite Oxide Nanoparticles with Diameter Greater than 20 Nm Are Biocompatible with Mouse Embryonic Stem Cells and Can Be Used in a Tissue Engineering System. *Small* **2014**, *10*, 1479−1484.
(27) Zhang, M.; Xu, R.; Xia, X.; Yang, Y.; Gu, J.; Qin, G.; Liu, X.; Ferrari, M.; Shen, H. Polycation-Functionalized Nanoporous Silicon Particles for Gene Silencing on Breast Cancer Cells. *Biomaterials* **2014**, *35*, 423−431.
(28) Climent, E.; Bernardos, A.; Martínez-Máñez, R.; Maquieira, A.; Marcos, M. D.; Pastor-Navarro, N.; Puchades, R.; Sancenón, F.; Soto, J.; Amorós, P. Controlled Delivery Systems Using Antibody-Capped Mesoporous Nanocontainers. *J. Am. Chem. Soc.* **2009**, *131*, 14075−14080.
(29) Lee, W.; Ji, R.; Gösele, U.; Nielsch, K. Fast Fabrication of Long-Range Ordered Porous Alumina Membranes by Hard Anodization. *Nat. Mater.* **2006**, *5*, 741−747.
(30) Li, Y.; Zheng, M.; Ma, L.; Shen, W. Fabrication of Highly Ordered Nanoporous Alumina Films by Stable High-Field Anodization. *Nanotechnology* **2006**, *17*, 5101−5105.
(31) Trivinho-Strixino, F.; Guerreiro, H. A.; Gomes, C. S.; Pereira, E. C.; Guimarães, F. E. G. Active Waveguide Effects from Porous Anodic Alumina: An Optical Sensor Proposition. *Appl. Phys. Lett.* **2010**, *97*, 011902.
(32) Wang, Y.; Santos, A.; Kaur, G.; Evdokiou, A.; Losic, D. Structurally Engineered Anodic Alumina Nanotubes as Nano-Carriers for Delivery of Anticancer Therapeutics. *Biomaterials* **2014**, *35*, 5517−5526.
(33) Wang, Y.; Kaur, G.; Zysk, A.; Liapis, V.; Hay, S.; Santos, A.; Losic, D.; Evdokiou, A. Systematic in Vitro Nanotoxicity Study on Anodic Alumina Nanotubes with Engineered Aspect Ratio: Understanding Nanotoxicity by a Nanomaterial Model. *Biomaterials* **2015**, *46*, 117−130.
(34) La Flamme, K. E.; Mor, G.; Gong, D.; La Tempa, T.; Fusaro, V. a; Grimes, C. a; Desai, T. a. Nanoporous Alumina Capsules for Cellular Macroencapsulation: Transport and Biocompatibility. *Diabetes Technol. Ther.* **2005**, *7*, 684−694.
(35) La Flamme, K. E.; Popat, K. C.; Leoni, L.; Markiewicz, E.; La Tempa, T. J.; Roman, B. B.; Grimes, C. A.; Desai, T. A. Biocompatibility of Nanoporous Alumina Membranes for Immunoisolation. *Biomaterials* **2007**, *28*, 2638−2645.
(36) Popat, K. C.; Mor, G.; Grimes, C. a; Desai, T. a. Surface Modification of Nanoporous Alumina Surfaces with Poly (Ethylene Glycol). *Langmuir* **2004**, *20*, 8035−8041.
(37) Low, S. P.; Williams, K. A.; Canham, L. T.; Voelcker, N. H. Evaluation of Mammalian Cell Adhesion on Surface-Modified Porous Silicon. *Biomaterials* **2006**, *27*, 4538−4546.
(38) Park, J.-H.; Gu, L.; von Maltzahn, G.; Ruoslahti, E.; Bhatia, S. N.; Sailor, M. J. Biodegradable Luminescent Porous Silicon Nanoparticles for in Vivo Applications. *Nat. Mater.* **2009**, *8*, 331−336.
(39) Santos, A.; Balderrama, V. S.; Alba, M.; Formentín, P.; Ferré-Borrull, J.; Pallarès, J.; Marsal, L. F. Nanoporous Anodic Alumina Barcodes: Toward Smart Optical Biosensors. *Adv. Mater.* **2012**, *24*, 1050−1054.
(40) Santos, A.; Alba, M.; Rahman, M. M.; Formentin, P.; Ferre-Borrull, J.; Pallares, J.; Marsal, L. F. Structural Tuning of Photoluminescence in Nanoporous Anodic Alumina by Hard Anodization in Oxalic and Malonic Acids. *Nanoscale Res. Lett.* **2012**, *7*, 228.

DOI: 10.1021/acsami.5b05016
ACS Appl. Mater. Interfaces 2015, 7, 18600−18608

(41) Macias, G.; Hernández-Eguía, L. P.; Ferré-Borrull, J.; Pallares, J.; Marsal, L. F. Gold-Coated Ordered Nanoporous Anodic Alumina Bilayers for Future Label-Free Interferometric Biosensors. *ACS Appl. Mater. Interfaces* **2013**, *5*, 8093−8098.
(42) Santos, A.; Ferré-Borrull, J.; Pallarès, J.; Marsal, L. F. Hierarchical Nanoporous Anodic Alumina Templates by Asymmetric Two-Step Anodization. *Phys. Status Solidi A* **2011**, *208*, 668−674.
(43) Kumeria, T.; Rahman, M. M.; Santos, A.; Ferré-Borrull, J.; Marsal, L. F.; Losic, D. Structural and Optical Nanoengineering of Nanoporous Anodic Alumina Rugate Filters for Real-Time and Label-Free Biosensing Applications. *Anal. Chem.* **2014**, *86*, 1837−1844.
(44) Mutalib Md Jani, A.; Anglin, E. J.; McInnes, S. J. P.; Losic, D.; Shapter, J. G.; Voelcker, N. H. Nanoporous Anodic Aluminium Oxide Membranes with Layered Surface Chemistry. *Chem. Commun.* **2009**, 3062−3064.
(45) Santos, A.; Formentín, P.; Pallarès, J.; Ferré-Borrull, J.; Marsal, L. F. Structural Engineering of Nanoporous Anodic Alumina Funnels with High Aspect Ratio. *J. Electroanal. Chem.* **2011**, *655*, 73−78.
(46) Furneaux, R. C.; Rigby, W. R.; Davidson, A. P. The Formation of Controlled-Porosity Membranes from Anodically Oxidized Aluminium. *Nature* **1989**, *337*, 147−149.
(47) Xiao, L.; Gu, L.; Howell, S. B.; Sailor, M. J. Porous Silicon Nanoparticle Photosensitizers for Singlet Oxygen and Their Phototoxicity against Cancer Cells. *ACS Nano* **2011**, *5*, 3651−3659.
(48) Secret, E.; Smith, K.; Dubljevic, V.; Moore, E.; Macardle, P.; Delalat, B.; Rogers, M. L.; Johns, T. G.; Durand, J. O.; Cunin, F.; Voelcker, N. H. Antibody-Functionalized Porous Silicon Nanoparticles for Vectorization of Hydrophobic Drugs. *Adv. Healthcare Mater.* **2013**, *2*, 718−727.
(49) Santos, A.; Macías, G.; Ferré-Borrull, J.; Pallarès, J.; Marsal, L. F. Photoluminescent Enzymatic Sensor Based on Nanoporous Anodic Alumina. *ACS Appl. Mater. Interfaces* **2012**, *4*, 3584−3588.
(50) Gu, Y.; Sun, W.; Wang, G.; Zimmermann, M. T.; Jernigan, R. L.; Fang, N. Revealing Rotational Modes of Functionalized Gold Nanorods on Live Cell Membranes. *Small* **2013**, *9*, 785−792.
(51) Luo, R.; Neu, B.; Venkatraman, S. S. Surface Functionalization of Nanoparticles to Control Cell Interactions and Drug Release. *Small* **2012**, *8*, 2585−2594.
(52) Alba, M.; Romano, E.; Formentín, P.; Eravuchira, P. J.; Ferré-Borrull, J.; Pallarès, J.; Marsal, L. F. Selective Dual-Side Functionalization of Hollow SiO_2 Micropillar Arrays for Biotechnological Applications. *RSC Adv.* **2014**, *4*, 11409−11416.
(53) Kuddannaya, S.; Chuah, Y. J.; Hui, M.; Lee, A.; Menon, N. V.; Kang, Y.; Zhang, Y. Surface Chemical Modification of Poly (dimethylsiloxane) for the Enhanced Adhesion and Proliferation of Mesenchymal Stem Cells. *ACS Appl. Mater. Interfaces* **2013**, *5*, 9777−9784.
(54) Moritz, M.; Łaniecki, M. SBA-15 Mesoporous Material Modified with APTES as the Carrier for 2-(3-Benzoylphenyl)propionic Acid. *Appl. Surf. Sci.* **2012**, *258*, 7523−7529.
(55) Qin, M.; Hou, S.; Wang, L.; Feng, X.; Wang, R.; Yang, Y.; Wang, C.; Yu, L.; Shao, B.; Qiao, M. Two Methods for Glass Surface Modification and Their Application in Protein Immobilization. *Colloids Surf., B* **2007**, *60*, 243−249.
(56) Li, W. Y.; Liu, J.; Chen, H.; Deng, Y.; Zhang, B.; Wang, Z.; Zhang, X.; Hong, S. Application of Oxalic Acid Cross-Linking Activated Alumina/chitosan Biocomposites in Defluoridation from Aqueous Solution. Investigation of Adsorption Mechanism. *Chem. Eng. J.* **2013**, *225*, 865−872.
(57) Jagtap, S.; Yenkie, M. K. N.; Labhsetwar, N.; Rayalu, S. Defluoridation of Drinking Water Using Chitosan Based Mesoporous Alumina. *Microporous Mesoporous Mater.* **2011**, *142*, 454−463.
(58) Silverstein, R. M.; Bassler, G. C.; Morrill, T. C. *Spectrometric Identification of Organic Compounds*, 4th ed.; John Wiley and Sons: New York, 1981.
(59) Sweetman, M. J.; Shearer, C. J.; Shapter, J. G.; Voelcker, N. H. Dual Silane Surface Functionalization for the Selective Attachment of Human Neuronal Cells to Porous Silicon. *Langmuir* **2011**, *27*, 9497−9503.
(60) Baranowska, M.; Slota, A. J.; Eravuchira, P. J.; Macias, G.; Xifré-Pérez, E.; Pallares, J.; Ferré-Borrull, J.; Marsal, L. F. Protein Attachment to Nanoporous Anodic Alumina for Biotechnological Applications: Influence of Pore Size, Protein Size and Functionalization Path. *Colloids Surf., B* **2014**, *122*, 375−383.
(61) Huang, D.; Li, Z.; Hu, H.; Cui, D. Synthesis and Characterization of Bovine Serum Albumin-Conjugated Copper Sulfide Nanocomposites. *J. Nanomater.* **2010**, *2010*, No. 641545.
(62) Bandekar, J. Amide Modes and Protein Conformation. *Biochim. Biophys. Acta, Protein Struct. Mol. Enzymol.* **1992**, *1120*, 123−143.
(63) Grdadolnik, J.; Maréchal, Y. Bovine Serum Albumin Observed by Infrared Spectrometry. I. Methodology, Structural Investigation, and Water Uptake. *Biopolymers* **2001**, *62*, 40−53.
(64) Servagent-Noinville, S.; Revault, M.; Quiquampoix, H.; Baron, M. Conformational Changes of Bovine Serum Albumin Induced by Adsorption on Different Clay Surfaces: FTIR Analysis. *J. Colloid Interface Sci.* **2000**, *221*, 273−283.
(65) Norde, W.; Giacomelli, C. E. BSA Structural Changes during Homomolecular Exchange between the Adsorbed and the Dissolved States. *J. Biotechnol.* **2000**, *79*, 259−268.
(66) Barbosa, L. R. S.; Ortore, M. G.; Spinozzi, F.; Mariani, P.; Bernstorff, S.; Itri, R. The Importance of Protein-Protein Interactions on the pH-Induced Conformational Changes of Bovine Serum Albumin: A Small-Angle X-Ray Scattering Study. *Biophys. J.* **2010**, *98*, 147−157.

DOI: 10.1021/acsami.5b05016
ACS Appl. Mater. Interfaces 2015, 7, 18600−18608